

Catalytic polysulfide conversion and physiochemical confinement for lithium–sulfur batteries

Sun, Zixu; Vijay, Sudarshan; Heenen, Hendrik H.; Eng, Alex Yong Sheng; Tu, Wenguang; Zhao, Yunxing; Koh, See Wee; Gao, Pingqi; Seh, Zhi Wei; Chan, Karen; Li, Hong

2020

Sun, Z., Vijay, S., Heenen, H. H., Eng, A. Y. S., Tu, W., Zhao, Y., . . . Li, H. (2020). Catalytic polysulfide conversion and physiochemical confinement for lithium–sulfur batteries. *Advanced Energy Materials*, 10(22), 1904010-. doi:10.1002/aenm.201904010

<https://hdl.handle.net/10356/142178>

<https://doi.org/10.1002/aenm.201904010>

This is the accepted version of the following article: Sun, Z., Vijay, S., Heenen, H. H., Eng, A. Y. S., Tu, W., Zhao, Y., . . . Li, H. (2020). Catalytic polysulfide conversion and physiochemical confinement for lithium–sulfur batteries. *Advanced Energy Materials*, 1904010-, which has been published in final form at <http://dx.doi.org/10.1002/aenm.201904010>. This article may be used for non-commercial purposes in accordance with the Wiley Self-Archiving Policy [<https://authorservices.wiley.com/authorresources/Journal-Authors/licensing/self-archiving.html>].

Catalytic Polysulfide Conversion and Physiochemical Confinement for Lithium-Sulfur Batteries

*Zixu Sun^{†1}, Sudarshan Vijay^{†2}, Hendrik H. Heenen^{†2}, Alex Yong Sheng Eng³, Wenguang Tu¹, Yunxing Zhao⁴, See Wee Koh¹, Pingqi Gao⁵, Zhi Wei Seh³, Karen Chan^{*2}, Hong Li^{*1,6,7}*

¹School of Mechanical and Aerospace Engineering, Nanyang Technological University, 639798, Singapore

²Catalysis Theory Center, Department of Physics, Technical University of Denmark, Lyngby, Denmark 2820

³Institute of Materials Research and Engineering, Agency for Science, Technology and Research (A*STAR), 2 Fusionopolis Way, Innovis, Singapore 138634, Singapore

⁵Ningbo Institute of Material Technology and Engineering, Chinese Academy of Sciences, Ningbo 315201, China

⁴School of Materials, Sun Yat-sen University, Guangzhou 510275, China

⁶Centre for Micro-/Nano-electronics (NOVITAS), School of Electrical and Electronic Engineering, Nanyang Technological University, 639798, Singapore

⁷CINTRA CNRS/NTU/THALES, UMI 3288, Research Techno Plaza, 637553, Singapore

[†]equal contribution

^{*}corresponding authors. Karen Chan: kchan@fysik.dtu.dk; Hong Li: ehongli@ntu.edu.sg

Keywords: lithium-sulfur batteries, catalytic polysulfide conversion, physicochemical confinement, hollow nanocage

Abstract

The lithium-sulfur (Li-S) battery is widely regarded as a promising energy storage device due to its low price and earth-abundant materials employed. However, the shuttle effect of lithium polysulfides (LiPSs) and sluggish redox conversion result in inefficient sulfur utilization, low power density, and rapid electrode deterioration. Herein, we address these challenges with two strategies (1) increasing LiPSs conversion kinetics through catalysis, and (2) alleviating the shuttle effect by enhanced trapping and adsorption of LiPSs. We achieve these improvements by constructing double-shelled hollow nanocages derived from core-shell metal organic frameworks, decorated with cobalt nitride catalyst. The N-doped hollow inner carbon shell not only serves as a physical trap and chemical absorber for LiPSs, but also improves the electrical conductivity of the electrode, resulting in a largely mitigated shuttle effect. Cobalt nitride (Co_4N) nanoparticles, embedded in nitrogen-doped carbon in the outer shell, catalyze the conversion of LiPSs, leading to decreased polarization and fast kinetics during cycling. Density functional theory simulations of the Li intercalation energetics confirm the improved catalytic activity of the Co_4N compared to metallic Co catalyst. Altogether, the double-shell hollow nanocage electrode shows large reversible capacity of 1242 mAh g^{-1} at 0.1 C, robust stability (a capacity retention of 658 mAh g^{-1} at 5 C after 400 cycles with low capacity fading of 0.04% per cycle), and superior cycling stability at high sulfur loading (4.5 mg cm^{-2}).

1. Introduction

Extensive efforts have been devoted to constructing the cathode of lithium-sulfur (Li-S) batteries to meet the ever-increasing energy demands due to the abundant reserves of materials involved, and affordable cost.^[1-3] However, the commercial application of [the sulfur cathode for](#) the Li-S batteries is restrained by several technical barriers^[4-6] compared with Li-ion battery.^[7] Firstly, the poor conductivity of sulfur and its reaction intermediates limit the sulfur utilization,^[8] thus lead to decreased energy density and power density. Secondly, during the charge/discharge process, there is a large volume change, resulting in rapid deterioration of the electrode structure. Various strategies have been investigated to increase electrode conductivity and to accommodate the volume expansion,^[9-11] Last but not least, the dissolution and transport of lithium polysulfides (LiPSs) in the electrolyte result in the fatal “shuttle effect” that causes the [deposition of Li₂S](#) on Li anode and [then degrades the cycle performance](#). This shuttle effect could be mitigated by (1) trapping/confining the soluble LiPSs in the cathode by physical and chemical adsorption,^[12-15] which prevents the transport of soluble LiPSs in the electrolyte, and (2) enhancing the kinetics of LiPS conversion reactions so that the soluble long-chain LiPS could transform to insoluble short-chain LiPS quickly, limiting the lifetime of soluble LiPS^[16, 17]. [Putting together, a superior Li-S battery could be achieved by designing a cathode with high electrical conductivity \(to facilitate electron transport\),^{\[18, 19\]} a porous structure \(to accommodate volume expansion\),^{\[9, 20\]} strong polar affinity for LiPSs \(to increase physiochemical adsorption\),^{\[18, 21, 22\]} and fast kinetics for LiPSs conversion \(to accelerate the reaction kinetics\)^{\[23\]}.](#)

Recent work has found that the use of a carbon support with properly designed structures can effectively mitigate the poor electrical conductivity of the cathode, serious volume expansion, as well the loss of soluble LiPSs,^[24-26] Various carbon-based hosts have been widely investigated as sulfur hosts, which physically confine LiPSs to enhance the electrochemical performance. Examples include graphene/graphene oxide^[27, 28], hollow

carbon^[25], carbon nanotubes (CNTs),^[24, 29, 30] carbon fibers,^[31] and porous carbon.^[26]

Generally, constructing three-dimensional (3D) porous carbon materials with abundant open access can effectively ensure high sulfur loading, efficient electrolyte infiltration, fast Li ion diffusion, and efficient electron transfer.^[32-35]

Nevertheless, the relatively weak interaction among carbon and LiPSs makes it difficult to trap the dissolved LiPSs.^[36, 37] Heteroatom doping into carbon frameworks has been proved to be an effective technique to improve the interaction between carbon host and LiPSs, as well as to enhance the electrical conductivity of carbon by doping-increased electrical charge density.^[5, 38-40] For example, Pan *et al.*^[40] prepared nitrogen-doped (N-) graphene nanohollows with 3D electronically conductive frameworks and strong interaction of LiPSs, which could increase the adsorption of LiPSs and maintain the structural integrity during cycling. An N, P-codoped carbon framework^[51] can effectively prevent LiPSs dissolution by physical trapping and chemical adsorption. An even stronger chemical adsorption of dissolved LiPSs can occur on polar metal-based compounds, such as metal oxides/sulfides.^[37, 41-44] However, these materials often have low electrical conductivities, which lead to poor electron transport.^[34] In addition, the transformation of LiPSs during the charge/discharge process also has slow kinetics on these materials, which result in poor rate performance.^[45] Additionally, some noble metals and metal phosphides as sulfur hosts are found to accelerate the reaction kinetics of LiPSs conversion.^[46, 47]

In this work, we introduce cobalt nitride (Co₄N)^[48, 49] as the catalyst to enhance the kinetics of LiPSs conversion. We embedded the Co₄N nanoparticles in N-doped carbon, which forms the outer shell of a double-shelled hollow nanocage whose inner shell is N-doped carbon (denoted as *h*-Co₄N@NC). Such a hollow nanocage not only enhances the sulfur loading, but also buffers the volume expansion of sulfur. Moreover, the N-doped inner shell can effectively trap the LiPSs by physical confinement and chemical adsorption.

Additionally, the Co₄N nanoparticles embedded in N-doped carbon outer shell can efficiently catalyze the reversible conversion of the polysulfide during charge/discharge cycling, as verified both experimentally and theoretically. The performances of the Co₄N catalyst are benchmarked against a cobalt-free nanocage (denoted as *h*-NC), and a metallic Co catalyst (denoted as *h*-Co@NC). Lastly, the N doping in carbon support can boost the conductivity of the integrated electrode. As a consequence, the electrode displays remarkable catalytic activity (low overpotential, small Tafel slope, and fast redox kinetics), high specific capacity (1242 mAh g⁻¹ at 0.1 C), and robust stability (a capacity retention of 658 mAh g⁻¹ at 5 C after 400 cycles), and excellent cycling stability at high sulfur loading.

2. Results and Discussion

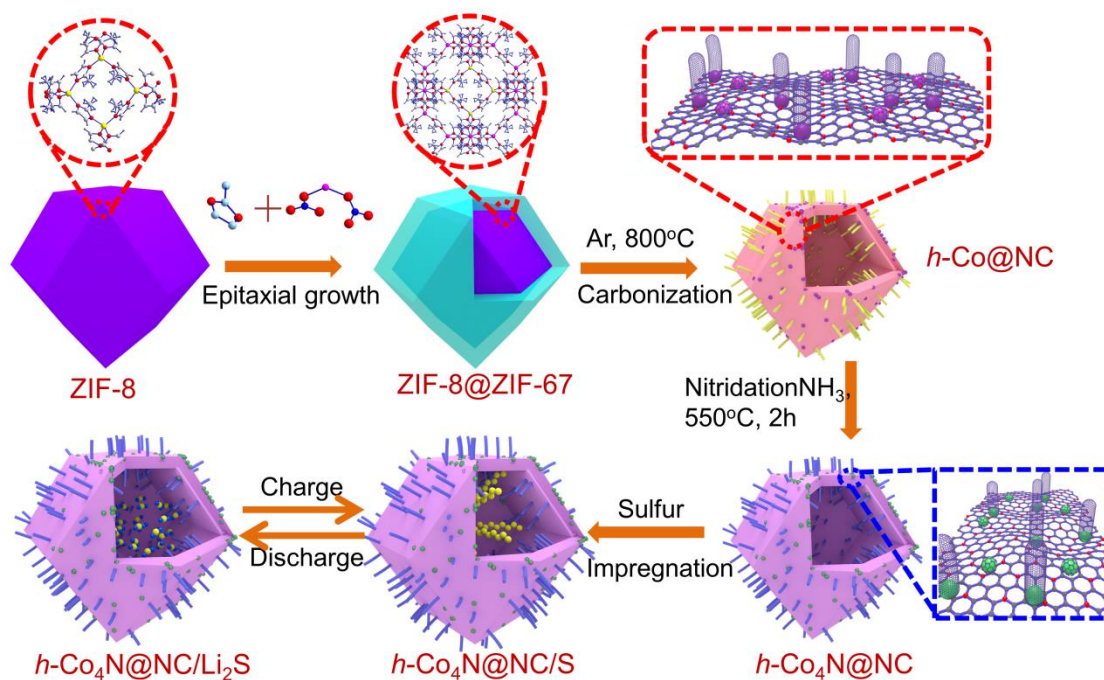


Figure 1 The synthesis process of the $h\text{-Co}_4\text{N@NC/S}$ electrode.

The preparation process of the $h\text{-Co}_4\text{N@NC/S}$ is shown in **Figure 1**. First, ZIF-8 was prepared at room temperature similar to a previous report.^[50] Then, with ZIF-8 as the template, a core-shelled ZIF-8@ZIF-67 structure was prepared via epitaxial growth using $\text{Co}(\text{NO}_3)_2 \cdot 6\text{H}_2\text{O}$ and 2-Methylimidazole as the precursors. A double-shell hollow architecture was obtained by pyrolysis of the core-shelled ZIF-8@ZIF-67 at 800 °C for 3 h in Ar atmosphere. Then, the harvested composite was further calcined at 600 °C for 2 h in NH_3 atmosphere. Finally, the $h\text{-Co}_4\text{N@NC/S}$ electrode was prepared by heating the mixture of $h\text{-Co}_4\text{N@NC}$ and sulfur. The XRD patterns and morphologies of the ZIF-8 and ZIF-67 crystals were shown in **Supporting Figure S1** and **Figure S2**, respectively. The ZIF-8 and ZIF-67 crystals with uniform sizes of 500 nm and 600 nm, respectively, have smooth surfaces.^[50, 51] After epitaxial growth, the ZIF-8@ZIF-67 was synthesized (Supporting Figure S2), which had the same morphology as that of ZIF-8. **Supporting Figure S3a** shows the TEM image of the ZIF-8@ZIF-67 structure, which confirms the polyhedral crystal and uniform sizes. The

composition of the composite was verified by the EDX elemental mapping, as shown in **Supporting Figure S3b**. All of the aforementioned characterizations suggest the successful formation of the ZIF-8@ZIF-67 structure.

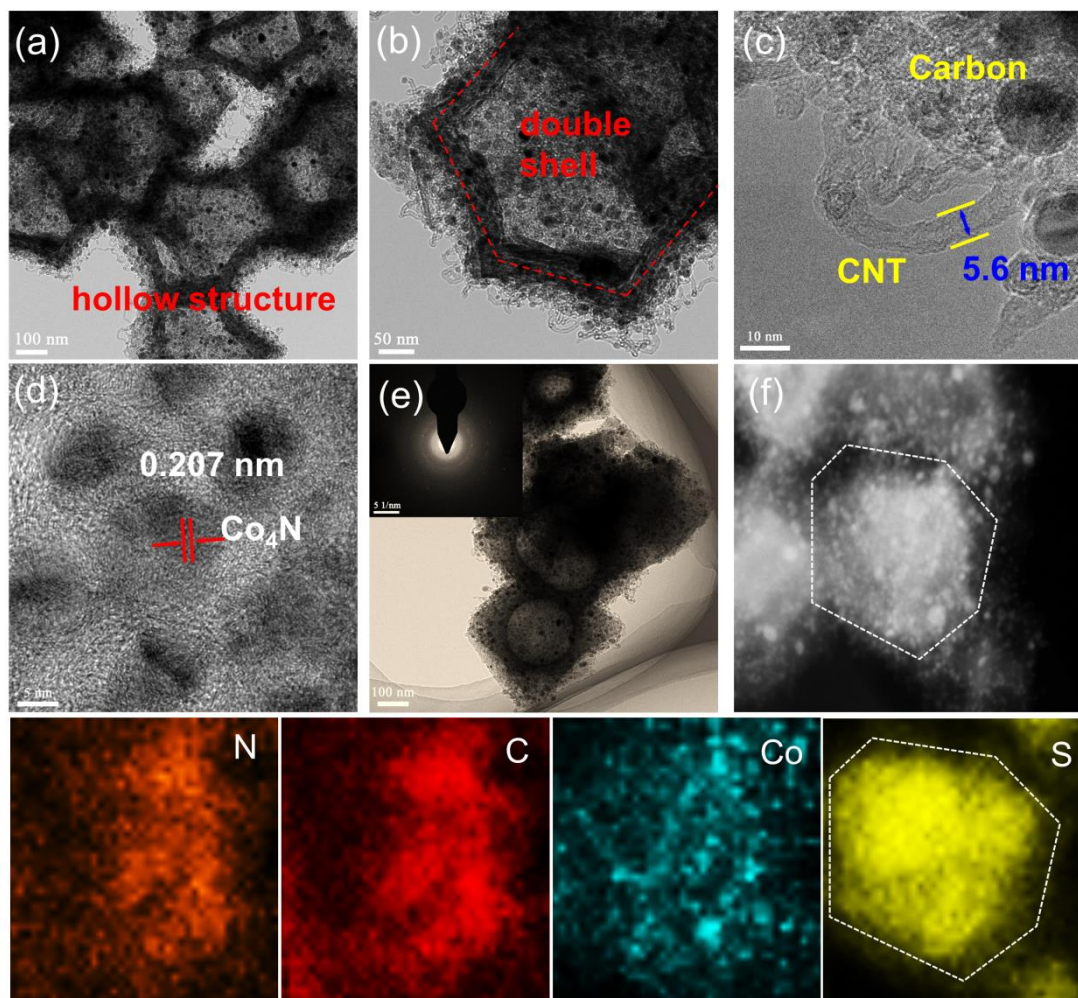


Figure 2 (a, b) TEM images of *h*-Co₄N@NC. (c, d) Typical HRTEM images of *h*-Co₄N@NC. (e) TEM image and SEAD pattern (inset) of *h*-Co₄N@NC/S. (f) HRTEM image of *h*-Co₄N@NC/S. (f) EDX element mapping images of *h*-Co₄N@NC/S. The shape of the particle is labeled with dotted polygons.

After pyrolysis, the core-shell structure turned into a hollow structure with abundant CNT grown on the surface catalysed by Co during pyrolysis, as shown in **Supporting Figure S4**. The polyhedral structure of the *h*-Co@NC remained but the crystal became smaller. The

XRD patterns of the *h*-Co@NC are shown in **Supporting Figure S5a**. One broad peak located at 26° is attributed to amorphous carbon, and two diffraction peaks centered at 44.25° and 51.55° match well with the (111) and (200) planes of metal Co^[51] (JCPDS#15-0806). There are no diffraction peaks of Zn-based compounds, indicating that Zn atoms were evaporated during high-temperature pyrolysis or Zn-based compounds may exist in amorphous state. After the acid etching, the diffraction peaks of Co metal in the *h*-Co@NC disappear (**Supporting Figure S5b**), indicating that the Co metal was completely removed. It is worth noting that the morphology has no apparent change compared with that of the *h*-Co@NC. TEM images of the *h*-Co@NC depicted in **Supporting Figure S6** show the double-shelled nanocage formation, which is in agreement with the SEM images. The inner shell is amorphous carbon, derived from ZIF-8. The outer shell of pyrolysed ZIF-67 is composed of CNT decorated with sub-10-nm Co nanoparticles (**Supporting Figure S6d**). After the nitridation process, the double-shelled morphologies of the polyhedral structure remained, as shown in **Supporting Figure S7**. TEM images of the *h*-Co₄N@NC are shown in **Figure 2a**, **2b**, which also display double-shelled structure with the N-doped carbon (inner shell) wrapped by the nanoparticle-decorated CNT (outer shell). The diameter of the N-doped CNT is about 5.6 nm (**Figure 2c**), which are uniformly distributed on the outer shell. The sub-10-nm nanoparticles on the outer shell are composed of Co₄N with lattice distance of about 0.207 nm (**Figure 2d** and **Supporting Figure S8**), corresponding to the (111) plane of Co₄N.^[52] After sulfur injection, the morphology remains unchanged (**Supporting Figure S9** and **Figure 2e**). The HRTEM image and its corresponding EDX elemental mapping in the dashed polygon (**Figure 2f**) show the distribution of N, C, Co and S elements. It is worth noting that N, C, and Co elements are homogeneously distributed in the box, however, S element distribution shows regular polygon shape, corresponding to the geometry of the

particle. This difference in element distribution suggests that sulfur nanoparticles are mainly confined inside the hollow nanocages.

XRD patterns of the *h*-Co@NC/S composite show the typical characteristic peaks of S₈ (JCPDS#08-0243) besides that of metal Co, compared with the patterns of the *h*-Co@NC (**Supporting Figure S10**). Also, the results of the XRD patterns of the *h*-Co₄N@NC/S have the same traits with that of the *h*-Co@NC/S composite (**Supporting Figure S11a**). The content of the sulfur in the *h*-Co₄N@NC/S is evaluated to be about 75.5wt% according to the TGA curve of the *h*-Co₄N@NC/S composite (**Supporting Figure S11b**). The BET specific surface area of the *h*-Co₄N@NC material is characterized to be around 576 m² g⁻¹ (**Supporting Figure S11c**), and the pore distribution ranges from 1 to 4 nm with the coexistence of micropores and mesopores (**Supporting Figure S11d**). After sulfur injection, the surface area of the composite decreases to 30 m² g⁻¹, and the fingerprint features of mesoporous structure disappear, suggesting that sulfur is filled into the hollow nanocages and mesopores. The Raman spectrum of the *h*-Co₄N@NC composite (**Supporting Figure S12a**) shows the presence of CNTs (RBM peak below 200 cm⁻¹), Co₄N (E_g, F_{2g} and A_{1g} peaks between 450 and 700 cm⁻¹), and doped/defective carbon (D and G peaks between 1200 and 1500 cm⁻¹). The XPS spectra of the *h*-Co₄N@NC sample confirm the presence of the Co, N, and C elements in the composite (**Supporting Figure S12b**). As shown in **Supporting Figure S12d**, the N 1s spectrum of the *h*-Co₄N@NC/S composite can be deconvoluted into pyridinic (398.6 eV), and graphitic N (401.8 eV).^[50] The presence of the N element could facilitate the LiPSs adsorption and accelerate the redox kinetics of the LiPSs, then favor the energy storage of the Li-S batteries.^[53, 54] In addition, the LiPSs adsorption capability of *h*-NC, *h*-Co@NC, and *h*-Co₄N@NC composites are compared in **Supporting Figure S13**. The quantitative comparison among the UV-vis spectra of the three solutions after the adsorption test is presented in **Figure S14**, with the bare Li₂S₆ solution as the reference. The UV-vis

spectra of the solution with added $h\text{-Co}_4\text{N@NC}$ after the adsorption test shows that the $h\text{-Co}_4\text{N@NC}$ sample has the highest adsorption capability. The much better adsorption capability of the $h\text{-Co}_4\text{N@NC}$ composite than the rest can be seen from the colorless solution, which also demonstrates the strong chemical affinity between LiPSs and Co_4N nanoparticles.

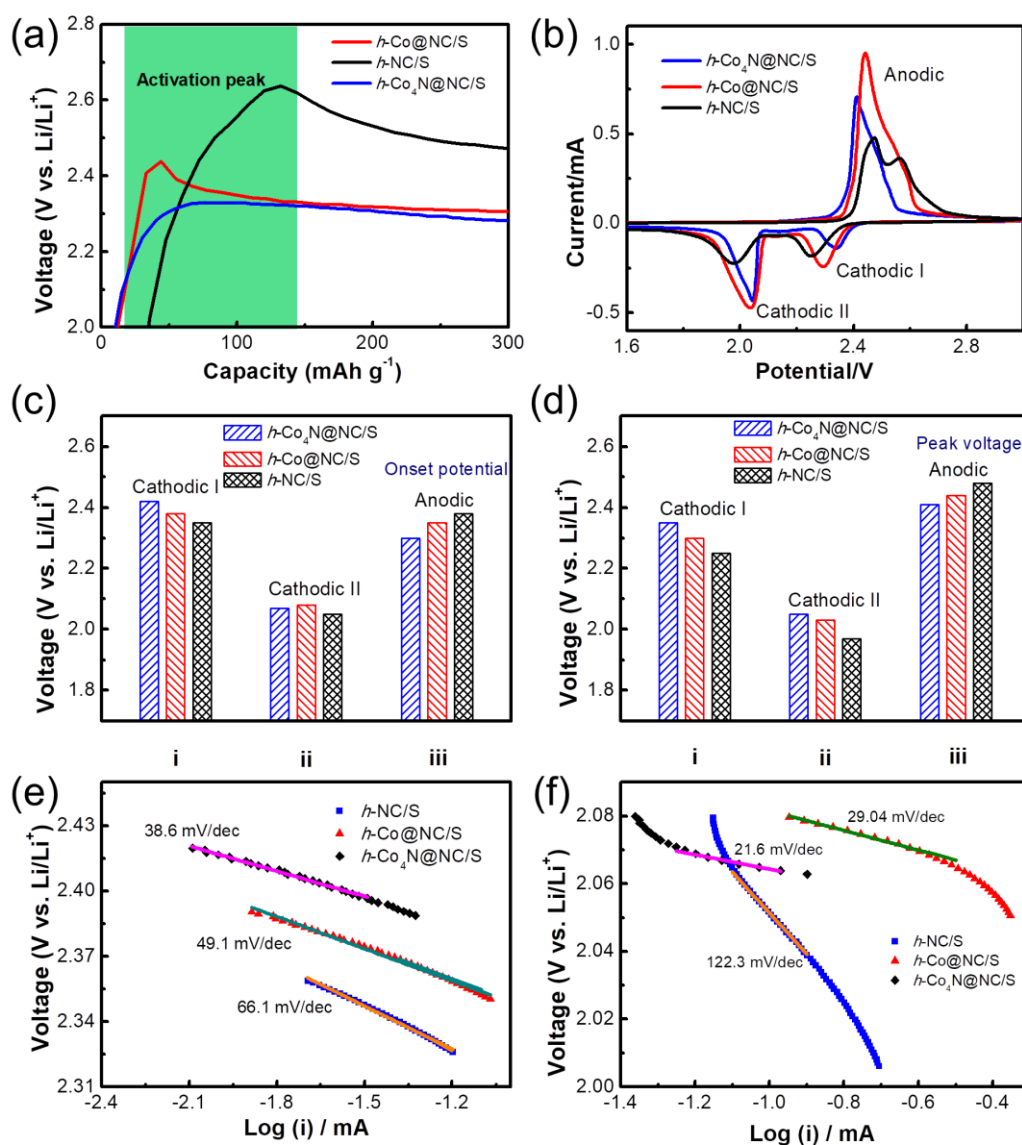


Figure 3 (a) First cycle charge voltage profiles of the $h\text{-NC/S}$, $h\text{-Co@NC/S}$, and $h\text{-Co}_4\text{N@NC/S}$ electrodes. (b) The first CV curves of the $h\text{-NC/S}$, $h\text{-Co@NC/S}$, and $h\text{-Co}_4\text{N@NC/S}$ electrodes. (c) Onset potential and (d) Peak voltage of the $h\text{-NC/S}$, $h\text{-Co@NC/S}$, and $h\text{-Co}_4\text{N@NC/S}$ electrodes from the first CV curves. (e, f) Tafel slopes of the

h-NC/S, *h*-Co@NC/S, and *h*-Co₄N@NC/S electrodes from the cathodic peaks of the first CV curves.

The aforementioned material characterizations confirm that we have successfully synthesized the double-shelled hollow nanocages with N-doped carbon as the inner shell, and Co₄N nanoparticle-embedded N-doped CNTs as the outer shell. Next, we discuss the electrochemical performance of the electrode. To verify the different activation barriers on the three composites, the first charge process is shown in **Figure 3a**. The *h*-Co₄N@NC/S electrode shows the lowest activation barrier as seen from the activation peak [that is the potential peak at the beginning of the first charge process^{\[55, 56\]}](#), suggesting the highest catalytic ability and the fastest redox kinetics. **Figure 3c** shows the onset potentials of the three electrodes according to the first CV curves (**Figure 3b**). The *h*-Co₄N@NC/S electrode shows the cathodic onset potentials of 2.42, and 2.07 V respectively, which are larger than those of the *h*-NC/S and *h*-Co@NC/S electrode. Furthermore, the anodic onset potential of the *h*-Co₄N@NC/S is 2.30 V, smaller than those of the *h*-NC/S and *h*-Co@NC/S electrode. Also, the trend of the peak potentials is similar to those of onset potentials (**Figure 3d**). In addition, the Tafel slopes of the three electrodes are shown in **Figure 3e** and **3f**, derived from the CV curves. During the cathodic and anodic processes, the *h*-Co₄N@NC/S electrode has the lowest Tafel slope among the three electrodes. The above results demonstrate that the *h*-Co₄N@NC can efficiently catalyze the conversion of the LiPSs and enhance the redox kinetics of LiPSs.

The catalytic effects of Co₄N were verified using density functional theory calculations. We investigated Li intercalation into S covered Co (101), Co₄N (111), and Co₄N (100) surfaces. Co(101) is the most abundant facet of metallic Co,^[57] while Co₄N(111) and Co₄N (100) are the Co₄N facets with the lowest surface energies (**Supplementary Table 1**). All three facets were highly reactive, and S₈ rings spontaneously dissociate completely to

separate S^* upon contact with the surface. The considerable stability of chemisorbed S^* atoms relative to physisorbed polysulfides is consistent with the reduced capacity losses during battery cycling. In what follows, we assume all S^* atoms in our model systems to be chemisorbed.

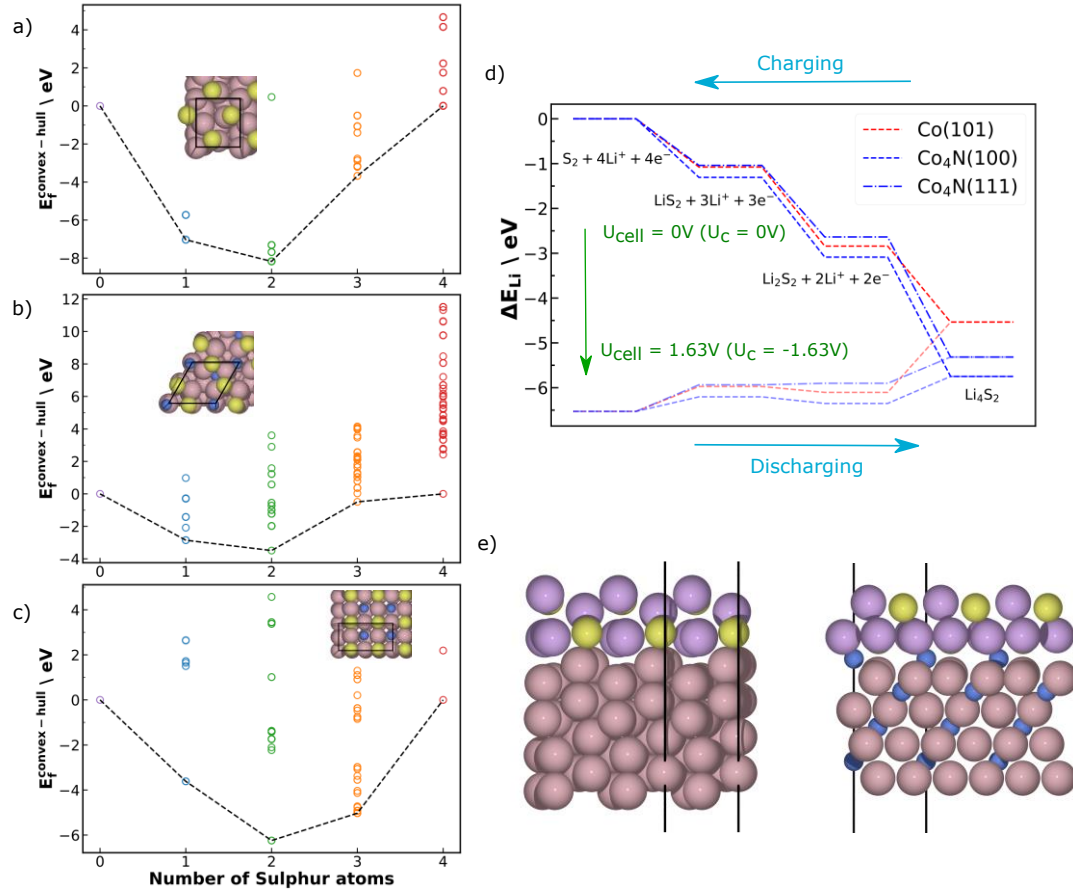


Figure 4 Sulfur coverage and potential dependence of Li intercalation of the Co and Co₄N catalysts from DFT simulations. (a-c) Convex hull depiction for S loading on Co(101), Co₄N(111), and Co₄N(100), respectively. The insets show the most stable S loading $x=2$ configuration for each surface. (d) Free energy pathway for lithiation on the considered surfaces at $x = 2$. The vertical arrow indicates the limiting cathodic potential $U_c = -1.63V$ at which lithiation becomes facile for Co₄N(111). The horizontal arrows indicate the charging and discharge processes. (e) Configurations of the most stable lithiated phases at a stoichiometry of Li_2S for Co(101) (left) and Co₄N(100) (right). Black lines indicate the unit cell.

Given the large configuration space for this multicomponent system, the S and mixed S/Li loadings were then systematically sampled for a substantial number of surface configurations of a given composition. Distance cut-offs based on preliminary sampling were imposed when generating initial structures (see details in Supplementary Information). The formation energies of the S loaded surfaces are depicted in **Figure 4a-c** as a convex hull representation computed as $E_f^{convex-hull}(S_xA) = E(S_xA) - xE(S_{lim}A) - (1-x)E(A)$ with $A=Co(101)_{slab}$, $Co_4N(111)_{slab}$, or $Co_4N(100)_{slab}$, and where S_{lim} is the respective maximum S coverage.^[58] For all surfaces, two S atoms ($x=2$) per unit cell yields the most thermodynamically stable loading. Electrically insulating surfaces of multi-layer S ($x>3$) are thermodynamically unfavorable. This suggests the surface is conductive as confirmed via density of state calculations (see **Supporting Figure S17, S18**).

Li intercalation on the different surfaces was sampled for the most stable configurations at the most favorable S loading ($x=2$). Corresponding minimum energy structures appeared to be very ordered, as depicted in **Figure 4e**. The free energy pathway constructed from the minimum energy structures for the catalyzed Li intercalation process is shown in **Figure 4d**. We find the trends in free energies for the lithiation of LiS to Li_2S are consistent with the experimentally determined cathodic CV peaks (**Figure 3b**). When the cell voltage is 0 V, the reaction pathway from an S^* covered surface to a surface with maximum lithiation is downhill in free energy. As the potential is increased, the reverse reaction starts to become favourable. At 1.63V, the reaction pathway corresponding to charging is completely exergonic for $Co_4N(111)$, but contains uphill steps for the other surfaces. This trend reflects a lower theoretical onset potential for Co_4N over Co, in agreement with the anodic peak position shown in Figure 3b, and confirms that Co_4N is a better redox catalyst. For all three facets considered, the catalyzed delithiation process is facile at the experimental cell potentials scanned ~2.0 V. [During discharging, a Li ion concentration gradient between the](#)

Co₄N or Co catalyst and the surrounding S covered N-doped graphene host material will build up. We hypothesize that this gradient equilibrates through Li diffusion and subsequent lithiation/de-lithiation via LiPS formation on the host material. This way, cycling will pass through the usual lithiation stages of S which is evident from the typical LiPS based cell potential profile. The better catalytic activity of Co₄N over Co may arise from the presence of N at the surface, which has unsaturated bonds that bind more strongly to the LiPS intermediates.

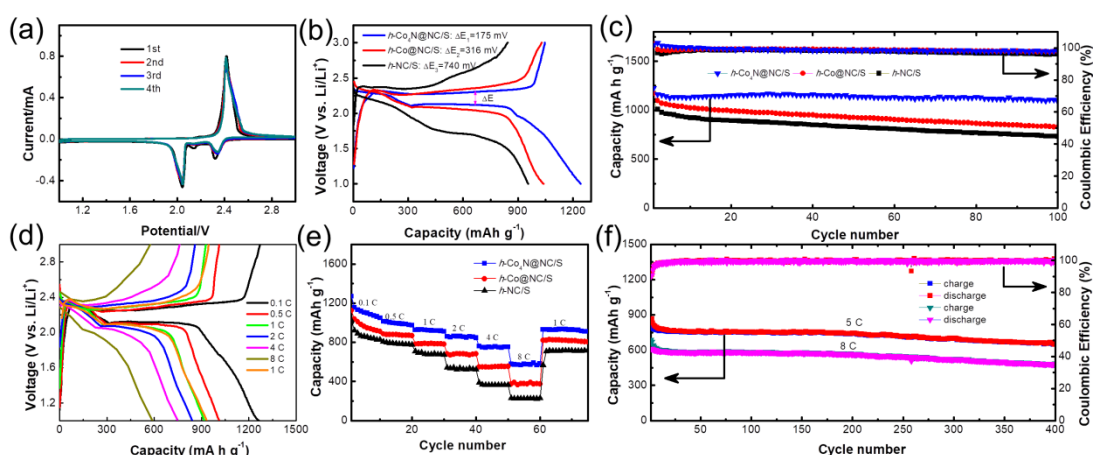


Figure 5 Electrochemical properties of Li-S batteries. (a) Cyclic voltammograms of *h*-Co₄N@NC/S electrodes for the first four cycles at 0.2 mV s⁻¹. (b) Representative charge-discharge voltage profiles. (c) Cycling at 0.1 C over 100 cycles of the *h*-NC/S, *h*-Co@NC/S, and *h*-Co₄N@NC/S electrodes with sulfur loading of 1.5 mg cm⁻². (d) Charge-discharge curves of the *h*-Co₄N@NC/S composites at various current densities from 0.1 C to 8 C. (e) Rate performance of the composites. (f) Cycling performance of the *h*-Co₄N@NC/S composite at high rates.

The electrochemical storage properties of the *h*-NC/S, *h*-Co@NC/S, and *h*-Co₄N@NC/S electrodes for Li-S batteries were characterized by coin cells employing a lithium plate as counter electrode. CV curves of the *h*-Co₄N@NC/S electrode are shown in **Figure 5a**. There

are two cathodic peaks centered at 2.33 and 2.04 V, respectively, which are attributed to the conversion of sulfur to LiPSs. In the oxidation process, there is a wide peak located at 2.42 V, corresponding to the reversible oxidation of LiPSs to $\text{Li}_2\text{S}_8/\text{S}$. **Supporting Figure S19a, S19b** show the typical CV curves of the other two electrodes, which also display two cathodic peaks and a broad anodic peak. However, the potentials of the reduction (oxidation) peaks for the *h*-NC/S and *h*-Co@NC/S electrodes are smaller (larger) than those of the *h*-Co₄N@NC/S material, which indicates much larger electrochemical polarization and slower kinetics. The CV profiles of the *h*-Co₄N@NC/S electrode for the first four cycles almost overlap, demonstrating the excellent stability. The first charge/discharge profiles of the three electrodes are shown in **Figure 5b** at 0.1 C. The charge/discharge capacities for the *h*-Co₄N@NC/S electrode are 1046 and 1242 mAh g⁻¹, respectively, which are the highest among the three electrodes. The *h*-Co₄N@NC/S electrode also shows the smallest ΔE , indicating the smallest electrochemical polarization, in agreement with the CV curves. The CV measurements were performed at different scan rates from 0.1 to 1.0 mV s⁻¹ to explore the kinetics of Li⁺ insertion/extraction and Li⁺ diffusion rate in the battery cell, as shown in **Figure S21** and **Figure S22**, which demonstrates that Li⁺ diffusion kinetics for the electrode is significantly enhanced by *h*-Co₄N@NC.

The above results demonstrate the fast reaction kinetics and the thermodynamically favorable conversion between LiPSs and $\text{Li}_2\text{S}_8/\text{S}$ on the *h*-Co₄N@NC/S composite. The latter also leads to excellent cycling stability over 100 cycles at 0.1 C, as displayed in **Figure 5c**. The first discharge capacity of the *h*-Co₄N@NC/S electrode is about 1246 mAh g⁻¹. In contrast, the *h*-NC/S and *h*-Co@NC/S electrodes deliver 951 and 1038 mAh g⁻¹, respectively. After 100 cycles, the capacity for the *h*-Co₄N@NC/S electrode still retains 1102 mAh g⁻¹ with coulombic efficiencies (CE) of almost 100%. In obvious contrast, the *h*-NC/S and *h*-Co@NC/S electrodes undergo fast capacity fade with low capacities of 726 and 835 mAh g⁻¹,

respectively, after 100 cycles. In addition, the h -Co₄N@NC/S electrode also delivers excellent rate capabilities, as shown in **Fig 5d** and **5e**. At the current rates from 0.1 to 8 C, the capacities of the h -Co₄N@NC/S electrode are 1272, 1014, 928, 856, 760 and 574 mAh g⁻¹, respectively, superior to those of the h -NC/S and h -Co@NC/S electrodes. Finally, when the current density returns to 1 C, the capacities of the h -NC/S, h -Co@NC/S, and h -Co₄N@NC/S electrodes are 712, 818 and 935 mAh g⁻¹, respectively, indicating the much better retention of the h -Co₄N@NC/S electrode. The much longer cycle life at high current rates for the h -Co₄N@NC/S electrode is depicted in **Figure 5f**. The first discharge capacities of the h -Co₄N@NC/S electrode at current rates of 5C and 8C are 786 and 609 mAh g⁻¹, respectively. After 400 cycles, the capacities of the electrode at 5C and 8C retain 658 and 481 mAh g⁻¹, respectively, with a CE of about 100%, displaying the excellent cycling stability.

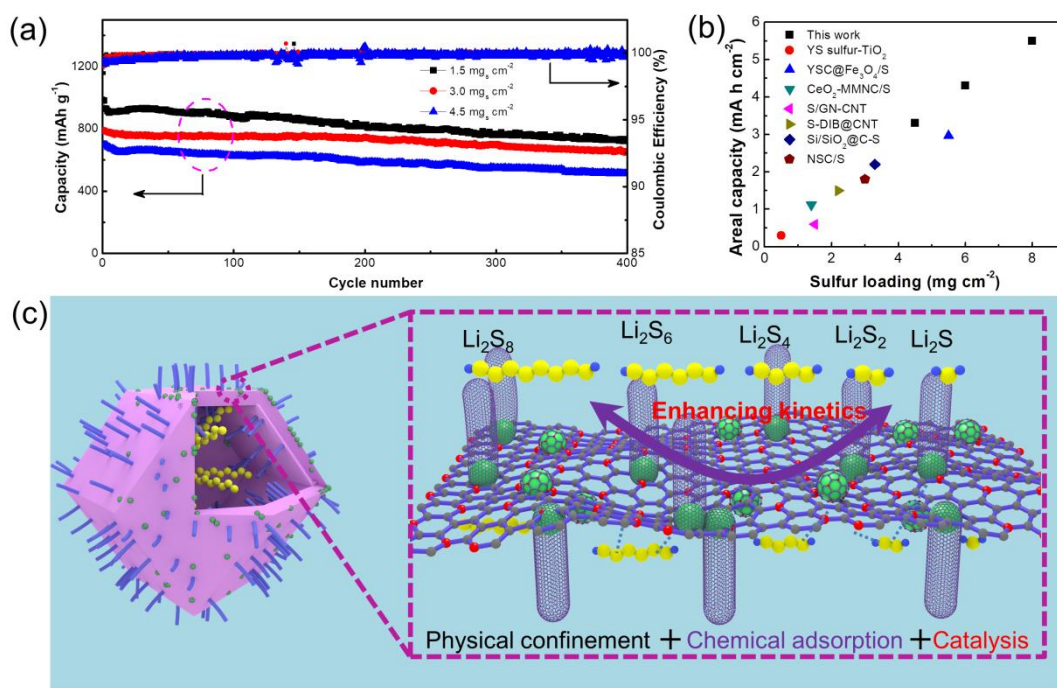


Figure 6 (a) Cycling performance of the h -Co₄N@NC/S composite with different sulfur loading. (b) Areal capacity and sulfur weight comparisons of the h -Co₄N@NC/S composites with the recent reports. (c) Schematic structure of the h -Co₄N@NC/S composite.

We further characterize the cycle properties with different sulfur loading to achieve the high-energy-density Li-S batteries, as displayed in **Figure 6a**. The *h*-Co₄N@NC/S electrode with different sulfur loadings of 1.5, 3.0 and 4.5 mg cm⁻² at 2C delivers capacities of 917, 783, and 707 mAh g⁻¹, respectively. After 400 cycles, the reversible capacities of the electrode still retain 729, 650 and 516 mAh g⁻¹, with high capacity retentions of 79.5%, 83.0% and 73.0%, respectively. The electrode with sulfur loading of 4.5 mg cm⁻² at 2C displays high initial areal capacity of 3.3 mAh cm⁻², which is superior to the most recent work (**Figure 6b**), such as S-DIB@CNT,^[30] CeO₂-MMNC/S,^[59] YSC@Fe₃O₄/S,^[60] and Si/SiO₂@C-S.^[61] In addition, as shown in **Figure S24**, the electrodes with sulfur loading of 6 and 8 mg, cm⁻² show excellent cycling performance with the areal capacity of around 4.3 and 5.5 mAh cm⁻², respectively. The superior electrochemical performance of the *h*-Co₄N@NC/S electrode is ascribed to the following factors (**Figure 6c**): (1) the double-shelled hollow nanocages can not only buffer the volume expansion of sulfur, but also promote electron transfer, ion diffusion, and electrolyte infiltration, (2) the N-doped carbon and CNTs shell can effectively improve the conductivity of the electrode and trap the LiPSs by physical confinement and chemical affinity, and (3) The homo-disperse Co₄N nanoparticles on the outer shell catalyzes the reversible conversion of the intermediates and accelerates the reversible conversion of the LiPSs.

3. Conclusion

In summary, we present a double-shelled hollow nanocage with N-doped carbon as the inner shell and Co₄N nanoparticles embedded within N-doped CNTs as the outer shell derived from the pyrolysis of the core-shell ZIF-8@ZIF-67. The 3D hollow double-shelled structure can effectively facilitate electron transfer, ion diffusion and electrolyte penetration. Co₄N nanoparticles catalyze LiPSs conversion, and reduce the shuttle effect by enhanced trapping and adsorption of LiPSs. Therefore, the *h*-Co₄N@NC/S electrode exhibited superior

electrochemical performance with a reversible capacity of 658 mAh g⁻¹ after 400 cycles in a low capacity-fading rate of 0.04% per cycle at a high rate of 5 C. Moreover, when increasing the sulfur loading to 4.5 mg cm⁻², the electrode also shows a high reversible capacity of 400 mAh g⁻¹ at 5 C after 400 cycles. This work exemplifies the rational design of high-performance Li-S batteries with unique catalyst electrode structure.

4. Experimental Section

Preparation of *h*-Co₄N@NC: 30 mL methanol with 48 mmol 2-Methylimidazole was added into 80 mL methanol with 12 mmol Zinc nitrate hexahydrate [Zn(NO₃)₂·6H₂O]. The mixture solution was aged for 24 h. Then, the ZIF-8 was collected by centrifugal treatment and dried at 70°C. 200 mg ZIF-8 was dispersed into 50 mL methanol. Then 400 mg cobaltous nitrate hexahydrate [Co(NO₃)₂·6H₂O] was dissolved into the solution. After sonication for 30 min, a 30 mL methanol solution with 12 mmol 2-methylimidazole was poured into the above suspension. After stirring for 24 h, the ZIF-8@ZIF-67 was prepared. The as-synthesized ZIF-8@ZIF-67 was pyrolysed at 800 °C for 3 h in Ar atmosphere, subsequent at 600 °C for 2 h in ammonia (NH₃) atmosphere, in order to obtain the double-shelled hollow nanocage with embedded Co nanoparticles (*h*-Co@NC). The control sample *h*-NC was prepared by etching *h*-Co@NC using a 6.0 M HCl solution. In contrast, the *h*-Co₄N@NC sample was obtained after nitridation of *h*-Co@NC. Lastly, to prepare the sulfur electrodes, the host materials were mixed with sulfur and heated at 155 °C for 10 h in a sealed vacuum tube.

Materials characterization: The X-ray powder diffraction (XRD) patterns of the materials were characterized by AXS D8 advance diffractometer. The X-ray photoelectron spectroscopy (XPS) was evaluated by Axis Ultra DLD. The morphologies of the materials were measured by a field emission scanning electron microscope (SEM) and a transmission electron microscope (TEM). The specific surface area and pore distribution of the samples

were tested by a Micromeritics ASAP 2020M adsorption analyzer. The sulfur content in the composite was evaluated by a Pyris diamond analyzer in Ar atmosphere.

Lithium LiPSs adsorption tests: To prepare Li_2S_6 solution, a S and Li_2S mixture with a molar ratio of 5:1 was dissolved into 1,2-dimethoxyethane (DME) and 1,3-dioxolane (DOL) solvents with a volume ratio of 1:1.

Electrochemical characterization: The electrodes were prepared using the synthesized catalyst material, conductive agent, and binder (PVDF) with a ratio of 8:1:1. The diameter of the electrode was about 16 mm. The thickness of the electrode was about 40 μm . The electrochemical performance of the electrodes was characterized by 2032 coin cells using a LAND test system. The charge/discharge profiles of the electrodes were carried out using the as-prepared sulfur composite as the cathode, the Li plate as the anode, 1M lithium bis(trifluoromethane) sulfonamide (LiTFSI) in DOL/DME containing 3% lithium nitrate (LiNO_3) as the electrolyte. CV curves were recorded at 5 mV s^{-1} at a potential range of 1.0-3.0 V. The as-prepared electrode was activated by three consecutive CV scans. Then, the electrochemical performances were characterized. Electrochemical impedance spectra were taken between 10 mHz and 1 MHz.

Density functional theory (DFT) calculations: All calculations were performed with the Vienna Ab Initio Simulation Package (VASP)^[62, 63] using the projector-augmented wave (PAW) method^[64] and a plane wave basis set in periodic boundary conditions. The RPBE^[65] functional was employed in combination with plane wave cutoff energies of 500 eV for all calculations. Lattice constants were determined using a $6\times 6\times 6$ Monkhorst-Pack k -point mesh. These settings produced lattice constants close to previous findings for both hcp-Co^[66] ($a=2.52 \text{ \AA}$, $c=4.05 \text{ \AA}$) and fcc-Co₄N^[67] (3.75 \AA). For surfaces, the Brillouin zone was sampled with a Monkhorst-Pack grid^[66] for 1×1 slab models of Co(101), Co₄N(111) and with $6\times 6\times 1$ k -point mesh. A 2×1 slab model was used for Co₄N(100) with a k -point mesh of

3×6×1. All slab models contained four atomic layers with the bottom two fixed. Gaussian smearing with a width of 0.1 eV was employed for all calculations. The electronic structure was converged until a total energy difference of 10^{-4} eV. To obtain minimum energy structures, geometries were relaxed until residual forces are less than 0.025 eV Å⁻¹. Periodic slab models were separated by a minimum vacuum of 16 Å. For the handling of atomistic models ASE^[68] and CatKit^[69] were employed.

Supporting Information

Supporting Information is available from the Wiley Online Library or from the author.

Acknowledgements

This work was supported by Nanyang Technological University under NAP award (M408050000) and Singapore Ministry of Education Tier 1 program (2018-T1-001-051).

S.V., H.H.H., and K.C. acknowledge a research grant (9455) from VILLUM FONDEN.

[Z.W.S acknowledges support from the Singapore National Research Foundation \(NRF-NRFF2017-04\)](#). Authors Zixu Sun, Sudarshan Vijay, Hendrik Heenen contributed equally to this work.

Conflict of Interest

The authors declare no conflict of interest.

Received: ((will be filled in by the editorial staff))

Revised: ((will be filled in by the editorial staff))

Published online: ((will be filled in by the editorial staff))

References

- [1] Kaiser, M.R., Z. Han, J. Liang, S.-X. Dou, and J. Wang, *Lithium sulfide-based cathode for lithium-ion/sulfur battery: Recent progress and challenges*. Energy Storage Materials, 2019. **19**: p. 1-15.
- [2] Zhang, L., Z. Chen, N. Dongfang, M. Li, C. Diao, Q. Wu, X. Chi, P. Jiang, Z. Zhao, L. Dong, R. Che, K.P. Loh, and H. Lu, *Nickel–Cobalt Double Hydroxide as a Multifunctional Mediator for Ultrahigh-Rate and Ultralong-Life Li–S Batteries*. Advanced Energy Materials, 2018. **8**(35): p. 1802431.
- [3] Kang, H., H. Kim, and M.J. Park, *Sulfur-Rich Polymers with Functional Linkers for High-Capacity and Fast-Charging Lithium-Sulfur Batteries*. Advanced Energy Materials, 2018: p. 1802423.
- [4] Xiao, P., F. Bu, G. Yang, Y. Zhang, and Y. Xu, *Integration of Graphene, Nano Sulfur, and Conducting Polymer into Compact, Flexible Lithium-Sulfur Battery Cathodes with Ultrahigh Volumetric Capacity and Superior Cycling Stability for Foldable Devices*. Adv Mater, 2017. **29**(40).
- [5] Wu, H., L. Xia, J. Ren, Q. Zheng, C. Xu, and D. Lin, *A high-efficiency N/P co-doped graphene/CNT@porous carbon hybrid matrix as a cathode host for high performance lithium–sulfur batteries*. Journal of Materials Chemistry A, 2017. **5**(38): p. 20458-20472.
- [6] Wu, X., N. Liu, M. Wang, Y. Qiu, B. Guan, D. Tian, Z. Guo, L. Fan, and N. Zhang, *A Class of Catalysts of BiOX (X = Cl, Br, I) for Anchoring Polysulfides and Accelerating Redox Reaction in Lithium Sulfur Batteries*. ACS Nano, 2019.
- [7] Zhang, K., H.-J. Kim, X. Shi, J.-T. Lee, J.-M. Choi, M.-S. Song, and J.H. Park, *Graphene/Acid Coassisted Synthesis of Ultrathin MoS₂ Nanosheets with Outstanding*

- Rate Capability for a Lithium Battery Anode*. Inorganic Chemistry, 2013. **52**(17): p. 9807-9812.
- [8] Samira, S., S. Deshpande, C.A. Roberts, A.M. Nacy, J. Kubal, K. Matesić, O. Oesterling, J. Greeley, and E. Nikolla, *Nonprecious Metal Catalysts for Tuning Discharge Product Distribution at Solid–Solid Interfaces of Aprotic Li–O₂ Batteries*. Chemistry of Materials, 2019. **31**(18): p. 7300-7310.
- [9] Zhong, Y., D. Chao, S. Deng, J. Zhan, R. Fang, Y. Xia, Y. Wang, X. Wang, X. Xia, and J. Tu, *Confining Sulfur in Integrated Composite Scaffold with Highly Porous Carbon Fibers/Vanadium Nitride Arrays for High-Performance Lithium-Sulfur Batteries*. Advanced Functional Materials, 2018: p. 1706391.
- [10] Li, M., Y. Wan, J.-K. Huang, A.H. Assen, C.-E. Hsiung, H. Jiang, Y. Han, M. Eddaoudi, Z. Lai, J. Ming, and L.-J. Li, *Metal–Organic Framework-Based Separators for Enhancing Li–S Battery Stability: Mechanism of Mitigating Polysulfide Diffusion*. ACS Energy Letters, 2017. **2**(10): p. 2362-2367.
- [11] Abbas, S.A., J. Ding, S.H. Wu, J. Fang, K.M. Boopathi, A. Mohapatra, L.W. Lee, P.C. Wang, C.C. Chang, and C.W. Chu, *Modified Separator Performing Dual Physical/Chemical Roles to Inhibit Polysulfide Shuttle Resulting in Ultrastable Li-S Batteries*. ACS Nano, 2017.
- [12] He, J., Y. Chen, W. Lv, K. Wen, C. Xu, W. Zhang, Y. Li, W. Qin, and W. He, *From Metal–Organic Framework to Li₂S@C–Co–N Nanoporous Architecture: A High-Capacity Cathode for Lithium–Sulfur Batteries*. ACS Nano, 2016. **10**(12): p. 10981-10987.
- [13] He, J., Y. Chen, and A. Manthiram, *Vertical Co₉S₈ hollow nanowall arrays grown on a Celgard separator as a multifunctional polysulfide barrier for high-performance Li–S batteries*. Energy & Environmental Science, 2018. **11**(9): p. 2560-2568.

- [14] He, J., W. Lv, Y. Chen, K. Wen, C. Xu, W. Zhang, Y. Li, W. Qin, and W. He, *Tellurium-Impregnated Porous Cobalt-Doped Carbon Polyhedra as Superior Cathodes for Lithium–Tellurium Batteries*. ACS Nano, 2017. **11**(8): p. 8144-8152.
- [15] He, J., W. Lv, Y. Chen, J. Xiong, K. Wen, C. Xu, W. Zhang, Y. Li, W. Qin, and W. He, *Direct impregnation of SeS₂ into a MOF-derived 3D nanoporous Co–N–C architecture towards superior rechargeable lithium batteries*. Journal of Materials Chemistry A, 2018. **6**(22): p. 10466-10473.
- [16] He, J., G. Hartmann, M. Lee, G.S. Hwang, Y. Chen, and A. Manthiram, *Freestanding 1T MoS₂/graphene heterostructures as a highly efficient electrocatalyst for lithium polysulfides in Li–S batteries*. Energy & Environmental Science, 2019. **12**(1): p. 344-350.
- [17] He, J., Y. Chen, and A. Manthiram, *Metal Sulfide-Decorated Carbon Sponge as a Highly Efficient Electrocatalyst and Absorbant for Polysulfide in High-Loading Li₂S Batteries*. Advanced Energy Materials, 2019. **9**(20): p. 1900584.
- [18] Li, Z., Q. He, X. Xu, Y. Zhao, X. Liu, C. Zhou, D. Ai, L. Xia, and L. Mai, *A 3D Nitrogen-Doped Graphene/TiN Nanowires Composite as a Strong Polysulfide Anchor for Lithium-Sulfur Batteries with Enhanced Rate Performance and High Areal Capacity*. Adv Mater, 2018: p. e1804089.
- [19] Yuan, H., H.-J. Peng, B.-Q. Li, J. Xie, L. Kong, M. Zhao, X. Chen, J.-Q. Huang, and Q. Zhang, *Conductive and Catalytic Triple-Phase Interfaces Enabling Uniform Nucleation in High-Rate Lithium-Sulfur Batteries*. Advanced Energy Materials, 2018: p. 1802768.
- [20] Lim, W.G., Y. Mun, A. Cho, C. Jo, S. Lee, J.W. Han, and J. Lee, *Synergistic Effect of Molecular-Type Electrocatalysts with Ultrahigh Pore Volume Carbon Microspheres for Lithium-Sulfur Batteries*. ACS Nano, 2018.

- [21] Ma, L., W. Zhang, L. Wang, Y. Hu, G. Zhu, Y. Wang, R. Chen, T. Chen, Z. Tie, J. Liu, and Z. Jin, *Strong Capillarity, Chemisorption, and Electrocatalytic Capability of Crisscrossed Nanostraws Enabled Flexible, High-Rate, and Long-Cycling Lithium-Sulfur Batteries*. ACS Nano, 2018. **12**(5): p. 4868-4876.
- [22] Gao, Z., Y. Schwab, Y. Zhang, N. Song, and X. Li, *Ferromagnetic Nanoparticle-Assisted Polysulfide Trapping for Enhanced Lithium-Sulfur Batteries*. Advanced Functional Materials, 2018. **28**(20): p. 1800563.
- [23] Xu, K., X. Liu, J. Liang, J. Cai, K. Zhang, Y. Lu, X. Wu, M. Zhu, Y. Liu, Y. Zhu, G. Wang, and Y. Qian, *Manipulating the Redox Kinetics of Li-S Chemistry by Tellurium Doping for Improved Li-S Batteries*. ACS Energy Letters, 2018. **3**(2): p. 420-427.
- [24] Ding, Y.-L., P. Kopold, K. Hahn, P.A. van Aken, J. Maier, and Y. Yu, *Facile Solid-State Growth of 3D Well-Interconnected Nitrogen-Rich Carbon Nanotube-Graphene Hybrid Architectures for Lithium-Sulfur Batteries*. Advanced Functional Materials, 2016. **26**(7): p. 1112-1119.
- [25] Zhang, J., C.P. Yang, Y.X. Yin, L.J. Wan, and Y.G. Guo, *Sulfur Encapsulated in Graphitic Carbon Nanocages for High-Rate and Long-Cycle Lithium-Sulfur Batteries*. Adv Mater, 2016. **28**(43): p. 9539-9544.
- [26] Chen, M., S. Jiang, C. Huang, X. Wang, S. Cai, K. Xiang, Y. Zhang, and J. Xue, *Honeycomb-like Nitrogen and Sulfur Dual-Doped Hierarchical Porous Biomass-Derived Carbon for Lithium-Sulfur Batteries*. ChemSusChem, 2017. **10**(8): p. 1803-1812.
- [27] Fei, L., X. Li, W. Bi, Z. Zhuo, W. Wei, L. Sun, W. Lu, X. Wu, K. Xie, C. Wu, H.L. Chan, and Y. Wang, *Graphene/sulfur hybrid nanosheets from a space-confined "sauna" reaction for high-performance lithium-sulfur batteries*. Adv Mater, 2015. **27**(39): p. 5936-42.

- [28] Chen, L., J. Feng, H. Zhou, C. Fu, G. Wang, L. Yang, C. Xu, Z. Chen, W. Yang, and Y. Kuang, *Hydrothermal preparation of nitrogen, boron co-doped curved graphene nanoribbons with high dopant amounts for high-performance lithium sulfur battery cathodes*. Journal of Materials Chemistry A, 2017. **5**(16): p. 7403-7415.
- [29] Cai, J., C. Wu, S. Yang, Y. Zhu, P.K. Shen, and K. Zhang, *Templated and Catalytic Fabrication of N-Doped Hierarchical Porous Carbon-Carbon Nanotube Hybrids as Host for Lithium-Sulfur Batteries*. ACS Appl Mater Interfaces, 2017. **9**(39): p. 33876-33886.
- [30] Hu, G., Z. Sun, C. Shi, R. Fang, J. Chen, P. Hou, C. Liu, H.M. Cheng, and F. Li, *A Sulfur-Rich Copolymer@CNT Hybrid Cathode with Dual-Confinement of Polysulfides for High-Performance Lithium-Sulfur Batteries*. Adv Mater, 2017. **29**(11).
- [31] Fang, R., S. Zhao, P. Hou, M. Cheng, S. Wang, H.M. Cheng, C. Liu, and F. Li, *3D Interconnected Electrode Materials with Ultrahigh Areal Sulfur Loading for Li-S Batteries*. Adv Mater, 2016. **28**(17): p. 3374-82.
- [32] Li, G., W. Lei, D. Luo, Y.-P. Deng, D. Wang, and Z. Chen, *3D Porous Carbon Sheets with Multidirectional Ion Pathways for Fast and Durable Lithium-Sulfur Batteries*. Advanced Energy Materials, 2017: p. 1702381.
- [33] Liu, Y., G. Li, Z. Chen, and X. Peng, *CNT-threaded N-doped porous carbon film as binder-free electrode for high-capacity supercapacitor and Li-S battery*. Journal of Materials Chemistry A, 2017. **5**(20): p. 9775-9784.
- [34] Xiang, M., H. Wu, H. Liu, J. Huang, Y. Zheng, L. Yang, P. Jing, Y. Zhang, S. Dou, and H. Liu, *A Flexible 3D Multifunctional MgO-Decorated Carbon Foam@CNTs Hybrid as Self-Supported Cathode for High-Performance Lithium-Sulfur Batteries*. Advanced Functional Materials, 2017. **27**(37): p. 1702573.

- [35] Gueon, D., J.T. Hwang, S.B. Yang, E. Cho, K. Sohn, D.K. Yang, and J.H. Moon, *Spherical Macroporous Carbon Nanotube Particles with Ultrahigh Sulfur Loading for Lithium-Sulfur Battery Cathodes*. ACS Nano, 2018.
- [36] Xiao, Z., Z. Yang, L. Zhang, H. Pan, and R. Wang, *Sandwich-Type NbS₂@S@I-Doped Graphene for High-Sulfur-Loaded, Ultrahigh-Rate, and Long-Life Lithium-Sulfur Batteries*. ACS Nano, 2017. **11**(8): p. 8488-8498.
- [37] Bao, W., L. Liu, C. Wang, S. Choi, D. Wang, and G. Wang, *Facile Synthesis of Crumpled Nitrogen-Doped MXene Nanosheets as a New Sulfur Host for Lithium-Sulfur Batteries*. Advanced Energy Materials, 2018. **8**(13): p. 1702485.
- [38] Chen, K., Z. Sun, R. Fang, Y. Shi, H.-M. Cheng, and F. Li, *Metal-Organic Frameworks (MOFs)-Derived Nitrogen-Doped Porous Carbon Anchored on Graphene with Multifunctional Effects for Lithium-Sulfur Batteries*. Advanced Functional Materials, 2018. **28**(38): p. 1707592.
- [39] Zhang, M., C. Yu, J. Yang, C. Zhao, Z. Ling, and J. Qiu, *Nitrogen-doped tubular/porous carbon channels implanted on graphene frameworks for multiple confinement of sulfur and polysulfides*. Journal of Materials Chemistry A, 2017. **5**(21): p. 10380-10386.
- [40] Tang, H., J. Yang, G. Zhang, C. Liu, H. Wang, Q. Zhao, J. Hu, Y. Duan, and F. Pan, *Self-assembled N-graphene nanohollows enabling ultrahigh energy density cathode for Li-S batteries*. Nanoscale, 2017. **10**(1): p. 386-395.
- [41] Chung, S.-H., L. Luo, and A. Manthiram, *TiS₂-Polysulfide Hybrid Cathode with High Sulfur Loading and Low Electrolyte Consumption for Lithium-Sulfur Batteries*. ACS Energy Letters, 2018. **3**(3): p. 568-573.

- [42] Chen, Y., S. Choi, D. Su, X. Gao, and G. Wang, *Self-standing sulfur cathodes enabled by 3D hierarchically porous titanium monoxide-graphene composite film for high-performance lithium-sulfur batteries*. Nano Energy, 2018. **47**: p. 331-339.
- [43] Cai, W., G. Li, D. Luo, G. Xiao, S. Zhu, Y. Zhao, Z. Chen, Y. Zhu, and Y. Qian, *The Dual-Play of 3D Conductive Scaffold Embedded with Co, N Codoped Hollow Polyhedra toward High-Performance Li-S Full Cell*. Advanced Energy Materials, 2018: p. 1802561.
- [44] Zhou, T., W. Lv, J. Li, G. Zhou, Y. Zhao, S. Fan, B. Liu, B. Li, F. Kang, and Q.-H. Yang, *Twinborn TiO₂-TiN heterostructures enabling smooth trapping-diffusion-conversion of polysulfides towards ultralong life lithium-sulfur batteries*. Energy & Environmental Science, 2017. **10**(7): p. 1694-1703.
- [45] Shao, H., F. Ai, W. Wang, H. Zhang, A. Wang, W. Feng, and Y. Huang, *Crab shell-derived nitrogen-doped micro-/mesoporous carbon as an effective separator coating for high energy lithium-sulfur batteries*. Journal of Materials Chemistry A, 2017. **5**(37): p. 19892-19900.
- [46] Al Salem, H., G. Babu, C.V. Rao, and L.M. Arava, *Electrocatalytic Polysulfide Traps for Controlling Redox Shuttle Process of Li-S Batteries*. J Am Chem Soc, 2015. **137**(36): p. 11542-5.
- [47] Yuan, H., X. Chen, G. Zhou, W. Zhang, J. Luo, H. Huang, Y. Gan, C. Liang, Y. Xia, J. Zhang, J. Wang, and X. Tao, *Efficient Activation of Li₂S by Transition Metal Phosphides Nanoparticles for Highly Stable Lithium-Sulfur Batteries*. ACS Energy Letters, 2017. **2**(7): p. 1711-1719.
- [48] Zhang, H., D. Tian, Z. Zhao, X. Liu, Y.-N. Hou, Y. Tang, J. Liang, Z. Zhang, X. Wang, and J. Qiu, *Cobalt nitride nanoparticles embedded in porous carbon nanosheet*

arrays propelling polysulfides conversion for highly stable lithium–sulfur batteries.

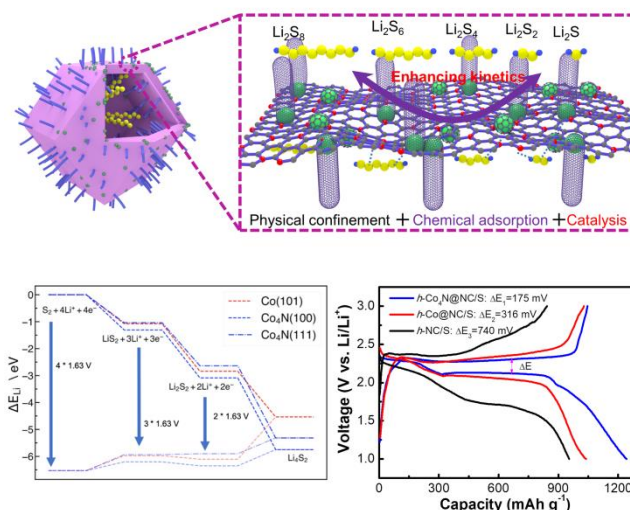
Energy Storage Materials, 2018.

- [49] Meng, F., H. Zhong, D. Bao, J. Yan, and X. Zhang, *In Situ Coupling of Strung Co₄N and Intertwined N-C Fibers toward Free-Standing Bifunctional Cathode for Robust, Efficient, and Flexible Zn-Air Batteries*. J Am Chem Soc, 2016. **138**(32): p. 10226-31.
- [50] Li, J., D. Yan, X. Zhang, S. Hou, T. Lu, Y. Yao, and L. Pan, *ZnS nanoparticles decorated on nitrogen-doped porous carbon polyhedra: a promising anode material for lithium-ion and sodium-ion batteries*. Journal of Materials Chemistry A, 2017. **5**(38): p. 20428-20438.
- [51] Li, X., Q. Jiang, S. Dou, L. Deng, J. Huo, and S. Wang, *ZIF-67-derived Co-NC@CoP-NC nanopolyhedra as an efficient bifunctional oxygen electrocatalyst*. Journal of Materials Chemistry A, 2016. **4**(41): p. 15836-15840.
- [52] Chen, P., K. Xu, Z. Fang, Y. Tong, J. Wu, X. Lu, X. Peng, H. Ding, C. Wu, and Y. Xie, *Metallic Co₄N Porous Nanowire Arrays Activated by Surface Oxidation as Electrocatalysts for the Oxygen Evolution Reaction*. Angew Chem Int Ed Engl, 2015. **54**(49): p. 14710-4.
- [53] Yu, Q., Y. Lu, R. Luo, X. Liu, K. Huo, J.-K. Kim, J. He, and Y. Luo, *In Situ Formation of Copper-Based Hosts Embedded within 3D N-Doped Hierarchically Porous Carbon Networks for Ultralong Cycle Lithium-Sulfur Batteries*. Advanced Functional Materials, 2018. **28**(39): p. 1804520.
- [54] Pang, Y., J. Wei, Y. Wang, and Y. Xia, *Synergetic Protective Effect of the Ultralight MWCNTs/NCQDs Modified Separator for Highly Stable Lithium-Sulfur Batteries*. Advanced Energy Materials, 2018: p. 1702288.

- [55] M. Wang, L. Fan, D. Tian, X. Wu, Y. Qiu, C. Zhao, B. Guan, Y. Wang, N. Zhang, K. Sun, *Rational Design of Hierarchical SnO₂/1T-MoS₂ Nanoarray Electrode for Ultralong-Life Li–S Batteries*. ACS Energy Letters, 2018. 3 (7): p. 1627-1633.
- [56] G. Zhou, H. Tian, Y. Jin, X. Tao, B. Liu, R. Zhang, Z. W. Seh, D. Zhuo, Y. Liu, J. Sun, J. Zhao, C. Zu, D. S. Wu, D. Q. Zhang, Y. Cui, *Catalytic oxidation of Li₂S on the surface of metal sulfides for Li-S batteries*. Proceedings of the National Academy of Sciences of the United States of America, 2017, 114 (5): p.840-845.
- [57] Tran, R., Z. Xu, B. Radhakrishnan, D. Winston, W. Sun, K.A. Persson, and S.P. Ong, *Surface energies of elemental crystals*. Scientific Data, 2016. 3(1): p. 160080.
- [58] Urban, A., D.-H. Seo, and G. Ceder, *Computational understanding of Li-ion batteries*. npj Computational Materials, 2016. 2(1): p. 16002.
- [59] Ma, L., R. Chen, G. Zhu, Y. Hu, Y. Wang, T. Chen, J. Liu, and Z. Jin, *Cerium Oxide Nanocrystal Embedded Bimodal Micromesoporous Nitrogen-Rich Carbon Nanospheres as Effective Sulfur Host for Lithium–Sulfur Batteries*. ACS Nano, 2017. 11(7): p. 7274-7283.
- [60] He, J., L. Luo, Y. Chen, and A. Manthiram, *Yolk-Shelled C@Fe₃O₄ Nanoboxes as Efficient Sulfur Hosts for High-Performance Lithium-Sulfur Batteries*. Adv Mater, 2017. 29(34).
- [61] Rehman, S., S. Guo, and Y. Hou, *Rational Design of Si/SiO₂ @Hierarchical Porous Carbon Spheres as Efficient Polysulfide Reservoirs for High-Performance Li-S Battery*. Adv Mater, 2016. 28(16): p. 3167-72.
- [62] Kresse, G. and J. Furthmüller, *Efficiency of ab-initio total energy calculations for metals and semiconductors using a plane-wave basis set*. Computational Materials Science, 1996. 6(1): p. 15-50.

- [63] Kresse, G. and J. Furthmüller, *Efficient iterative schemes for ab initio total-energy calculations using a plane-wave basis set*. Physical Review B, 1996. **54**(16): p. 11169-11186.
- [64] Blöchl, P.E., *Projector augmented-wave method*. Physical Review B, 1994. **50**(24): p. 17953-17979.
- [65] Hammer, B., L.B. Hansen, and J.K. Nørskov, *Improved adsorption energetics within density-functional theory using revised Perdew-Burke-Ernzerhof functionals*. Physical Review B, 1999. **59**(11): p. 7413-7421.
- [66] Monkhorst, H.J. and J.D. Pack, *Special points for Brillouin-zone integrations*. Physical Review B, 1976. **13**(12): p. 5188-5192.
- [67] Matar, S.F., A. Houari, and M.A. Belkhir, *Ab initio studies of magnetic properties of cobalt and tetracobalt nitride $\mathrm{Co}_4\mathrm{N}$* . Physical Review B, 2007. **75**(24): p. 245109.
- [68] Hjorth Larsen, A., J. Jørgen Mortensen, J. Blomqvist, I.E. Castelli, R. Christensen, M. Dułak, J. Friis, M.N. Groves, B. Hammer, C. Hargus, E.D. Hermes, P.C. Jennings, P. Bjerre Jensen, J. Kermode, J.R. Kitchin, E. Leonhard Kolsbjerg, J. Kubal, K. Kaasbjerg, S. Lysgaard, J. Bergmann Maronsson, T. Maxson, T. Olsen, L. Pastewka, A. Peterson, C. Rostgaard, J. Schiøtz, O. Schütt, M. Strange, K.S. Thygesen, T. Vegge, L. Vilhelmsen, M. Walter, Z. Zeng, and K.W. Jacobsen, *The atomic simulation environment—a Python library for working with atoms*. Journal of Physics: Condensed Matter, 2017. **29**(27): p. 273002.
- [69] Boes, J.R., O. Mamun, K. Winther, and T. Bligaard, *Graph Theory Approach to High-Throughput Surface Adsorption Structure Generation*. The Journal of Physical Chemistry A, 2019. **123**(11): p. 2281-2285.

TOC: A double-shelled hollow nanocage decorated with cobalt nitride embedded in nitrogen-doped carbon is employed as the cathode for lithium sulfur battery. Cobalt nitride efficiently catalyzes polysulfide conversion. The porous and hollow structure facilitates physiochemical polysulfide adsorption, and effectively accommodate volume expansion. As a result, the shuttle of polysulfide in lithium sulfur battery is greatly suppressed.



Keyword : lithium-sulfur batteries, catalytic polysulfide conversion, physicochemical confinement, hollow nanocage

Zixu Sun^{†1}, Sudarshan Vijay^{†2}, Hendrik H. Heenen^{†2}, Alex Yong Sheng Eng³, Wenguang Tu¹, Yunxing Zhao⁴, See Wee Koh¹, Pingqi Gao⁵, Zhi Wei Seh³, Karen Chan^{*2}, Hong Li^{*1,6,7}

Title: Catalytic Polysulfide Conversion and Physiochemical Confinement for Lithium-Sulfur Batteries